



Machinability of partition milling stainless steel/Inconel functionally gradient material printed with directed energy deposition

Benquan Li¹ · Runyu Zhang¹ · Arif Malik¹ · Wei Li¹ 

Received: 9 June 2022 / Accepted: 6 September 2022 / Published online: 10 September 2022
© The Author(s), under exclusive licence to Springer-Verlag London Ltd., part of Springer Nature 2022

Abstract

As functionally gradient materials (FGMs) reveal innovative mechanical properties, they have aroused huge interest in multiple industry areas. In this study, a hybrid manufacturing (HM) technique that combines a directed energy deposition (DED)-type additive manufacturing (AM) fabrication process with milling-type machining is investigated. In the DED process examined, Inconel 718 (IN718) and stainless steel 316L (SS316L) metal powders were blown into the molten pool at different and varying respective flow rates to achieve specific composition ratios for different printed layers so that a smooth gradient transition from SS316L to IN718 was achieved. Due to the attendant generation of rough surfaces common to such FGMs, partition milling was employed after fabrication, and the cutting temperatures and forces were simultaneously recorded considering the significant anisotropy in mechanical properties. The surface roughness of each FGM gradient section and tool wear mechanism were also measured after machining. Through analysis of the experimental results, the machining mechanism was revealed, which provides new insights into the machinability of SS316L/IN718 FGMs.

Keywords Functionally gradient material · Machining · Directed energy deposition · Hybrid manufacturing

1 Introduction

Functionally graded materials (FGMs) are characterized by the gradual gradient transition among multiple material compositions over the volume of FGM specimens, which is reflected by the corresponding variation in the mechanical properties of the FGMs. Because the mechanical properties vary with spatial location, an FGM part is able to simultaneously support different mechanical loads imposed at different locations, which is uniquely advantageous over more traditional, relatively homogeneous alloys. In addition, FGMs exhibit smooth variations in material, eliminating the sharp transition where stress concentrations may occur. Thus, compared to the jointing of multiple dissimilar materials by welding on edges, the absence of sharp transition interfaces makes FGMs more functional and ensures longer service life [1–3].

To manufacture FGMs, directed energy deposition (DED) has been an efficient and prevalent technology, not only

because of its rapid advancement in recent years [4] but also because the fabrication mechanism is suited to the construction of FGMs. During the DED printing process, the dissimilar metal powders are blown into the molten pool synchronously under the pressure of compressed inert gas. Since the feed rate of the deposited materials can be readily adjusted using G-Code, the weight ratio of combined metal powder on each layer can also be changed. In such manner, smooth variations in layer compositions along the build direction can be realized. Accordingly, research regarding fabrication and characterization of FGMs has become increasingly prevalent. Li et al. recently fabricated Inconel-steel functionally graded bimetal materials using DED. Through a series of tests of microstructure, chemistry, phase composition, element segregation, and microhardness, the excellent properties of these DED-built FGMs were confirmed [5]. Kim et al. evaluated FGMs composed of IN718 and SS316L in terms of microstructural transformation, defect behavior, and Vickers hardness, and concluded that removal of the defective compositional range helped obtain a robust FGM without noticeable defects [6]. Additionally, in previous research, Banait et al. successfully used DED to construct FGMs composed of Ni–Cr–B–Si and SS316L, which was followed by heat treatment. The microstructures, hardness, ductility, and

✉ Wei Li
Wei.Li@UTDallas.edu

¹ Mechanical Engineering, The University of Texas at Dallas, Richardson, TX, USA

energy storage of the FGMs were evaluated, and revealed that heat treatment improved the energy absorbing capacity of the graded deposit [7].

A major impediment of the 3D printed metal parts in general is that they are always rough on the outer surface, and they possess lower fabrication accuracy compared to those made using conventional subtractive manufacturing technologies. In this context, machining, as a posttreatment method, is also essential to enhance the performance of AM-built FGMs [8–11]. Such a combined manufacturing technique that effectively converges additive and subtractive operations to create a single manufacturing workflow constitutes a promising hybrid manufacturing (HM) technology [12–14]. However, while computer numerical control (CNC) of milling has been used for decades in industry, little research has been done on the milling of FGMs, and specifically to investigate the machinability of DED-built FGMs. Since the post-AM machining process is indispensable for FGMs, to achieve functional requirements such as dimensional accuracy and surface finish, there exists an urgent need for researchers to address FGM machinability.

In this study, IN718 and SS316L were selected as the two FGM compositions for investigation. As is well known, IN718 is distinguished from the other metals due to its oxidation and corrosion resistance, making it well suited for functioning in extreme environments under load. IN718 is also able to withstand high temperatures approaching its melting point [15]. Accordingly, IN718 is widely utilized in various applications within the aerospace industry and in nuclear reactors. SS316L is relatively affordable compared to other materials and possesses good weldability, because of which SS316L is widely used in both engineering and consumer applications. In this research, these two alloy powders were melted by a laser beam and deposited as FGMs. The gradual gradient distribution between IN718 and SS316L was then verified using energy dispersive X-ray spectroscopy (EDS) testing. In addition, milling operations on each gradient section of the FGMs were conducted, and the resulting surface roughness, cutting temperature, and cutting force and tool wear mechanism were analyzed. Through the results obtained from these milling experiments, the machinability of SS316L/IN718 FGMs was investigated and summarized, contributing to the further development and application of FGMs.

2 Experimental procedures

2.1 Direct energy deposition

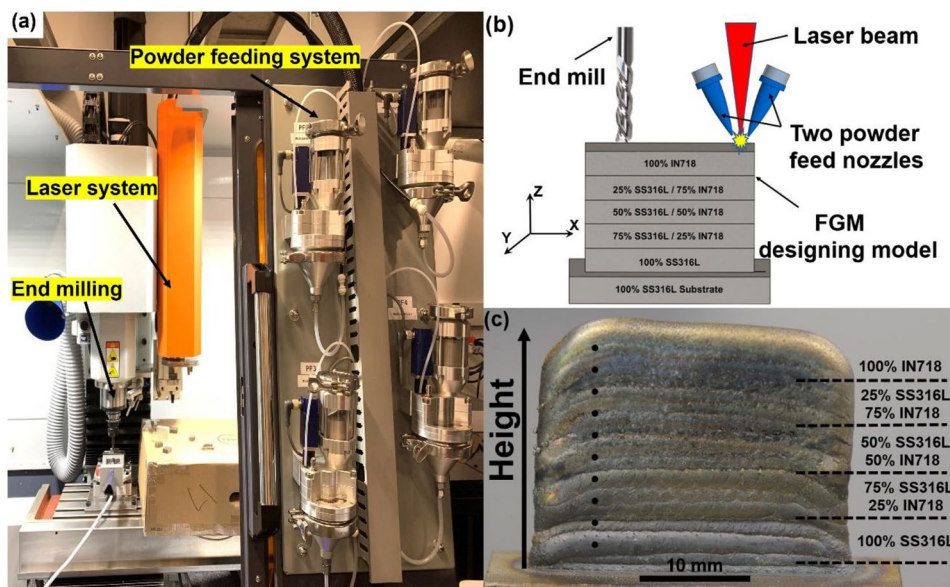
The FGM specimens fabricated and machined were composed of two metal alloy powders, namely IN718 and SS316L (PowderRange, Carpenter Additive). The gas atomized alloy powder, with a particle size between 45 and 106 μm , was used as feedstock material. The main chemical elements and their weight ratios in the alloy powder are listed in Table 1. The DED process was accomplished using a custom hybrid manufacturing platform in which a CNC milling machine (Tormach 1100 M) was integrated with a laser source (Laserline GmbH, LDM 1000–40) and a powder feeder system. As shown in Fig. 1a, the HM platform is equipped with 4 separate powder feeder counts, and delivers a laser power up to 1 kW. A schematic model of the FGM structure for this research, and the HM process configuration, is shown in Fig. 1b in which five material gradients were assigned. The first material gradient section to be printed constitutes a 100% SS316L region, consistent with the substrate material. In each of the successive material gradient sections, the weight ratio of SS316L was reduced 25% while the IN718 was correspondingly increased 25% until the top gradient section reached 100% IN718. During the printing process, the IN718 and SS316L powders were blown from the feeder counts separately by protective argon gas with a feed rate of 4 L/min. The metal powder was melted by the laser beam and deposited layer by layer onto the SS316L substrate, with the inert gas argon protecting the molten metal from oxidation. Through adjusting the individual feed rates of the two powders, the specific composition ratios assigned for the five gradient sections were achieved. Each printing layer was set to 1.016 mm height and the FGM contained 20 layers in total. The overall printed specimen thus represented a thin-walled part of 22.5 mm height and 29 mm length, as shown in Fig. 1c. Although no cracks were observed, it was clear that dimensional accuracy of the FGM specimen would not qualify for end use application since the exterior surfaces produced by the DED were irregular, and the boundaries between adjacent layers were dimensionally evident. As such, post-build machining is of huge significance so that the surfaces characterized by “ripple” morphology from the DED process can be removed, and the surface roughness significantly improved.

To verify the gradient variation between SS316L and IN718 along the build-up direction, EDS tests were performed

Table 1 The element composition in the alloy powder of SS316L and IN718 (wt.%)

Composition	Fe	Cr	Ni	Mn	Mo	Nb+Ta	N	Si	C	P	Co	Cu	Ti	S
SS 316L	Bal.	16–18	10–14	2	2–3	-	0.1	1	0.03	0.05	-	-	-	0.03
In 718	Bal.	17–21	50–55	0.35	2.8–3.3	4.75–5.5	0.03	0.15	0.02–0.08	0.02	1	0.3	0.75–1.15	-

Fig. 1 **a** The experimental HM setup in which DED and milling were performed. **b** Model of the FGM structure for this research, and the HM process configuration. Note: the z-axis is the build-up direction. The composition in the FGMs was gradually transferred from the 100% SS316L substrate and the first established 100% SS316L material section on it, to 100% IN718 through three transition sections, as shown. **c** FGMs shown after the DED process. The black dots shown from the bottom to the top area identify the positions where EDS tests were conducted



on the outer surface of printed FGMs to analyze the weight ratio and distribution of Fe, Ni, and Cr elements in the formation of the gradient change. The reason why these three chemical elements were selected is that their weight ratios were higher than other elements among the two types of alloy powder (Table 1). Ten locations were selected along the build-up direction for EDS testing, as schematically illustrated by the black dots in Fig. 1c. Within each material gradient, two test points were assigned. The sequence number of tested positions ranged from 1 to 10 as the height increased, starting from the 100% SS316L section at the bottom to the 100% IN718 region at the top.

2.2 Machinability test

2.2.1 Milling setup and strategies

In this paper, partition milling is introduced to machine FGMs produced by DED, as illustrated in Fig. 2. The milling processes

were performed using a vertical CNC milling machine (Tormach 1100 M) while the milling cutters employed in this study were tungsten carbide uncoated square end mills (MSC Industrial Direct Co., Inc.) with 4-flutes, 30° helix-angle, and 3/8-in diameter.

In the partition milling strategy (Fig. 2a), each composition gradient section was machined separately instead of simultaneously. The spindle speed was set at 2000 rpm, with a feed rate of 0.5 in/min, while radial depth of cut (a_{rc}) was 1 mm, and axial depth of cut (a_{ap}) was 3 mm. All cutting parameters were programmed in a G-code file and are summarized in Table 2. Since FGM specimens generally have hard outer surfaces, up milling was employed in both milling schemes to avoid machine chatter and maintain cutting stability during the milling operations.

The surfaces of the machined FGM workpiece are illustrated in Fig. 2b. Parallel milling tracks can be seen on the FGM specimen, which indicates that a partition milling scheme was adopted. Considering that FGM workpiece had

Fig. 2 **a** The partition milling setup is shown, where the milling paths are indicated by the orange arrows, and which shows five gradient regions to be machined in turn from top to bottom. **b** Image of machined surfaces when employing partition milling scheme

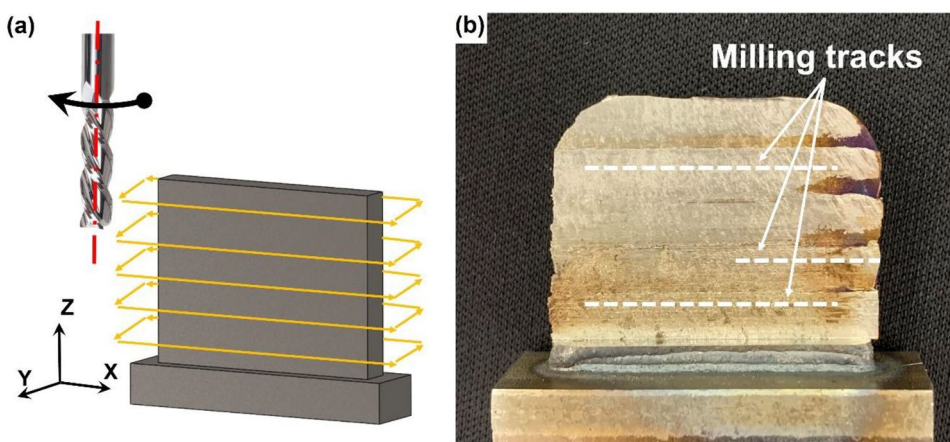


Table 2 The parameters used in two milling strategies

Cutting parameters (unit)	Value
Spindle speed (rpm)	2000
Feed rate (in/min)	0.5
Radial depth of cut (mm)	1
Axial depth of cut (mm)	3

an obvious irregular topography on the exterior, and poor dimensional tolerance caused by DED process, the actual radial depth of each milling trial in the partition milling strategy was slightly different. Consequently, each cutting region was bounded by parallel milling tracks.

2.2.2 Surface roughness evaluation

Since the material composition in FGMs is not uniform but includes a gradient distribution along build-up direction, mechanical properties such as hardness and strength are also not constant on the cutting layers. Thus, the roughness of machined surfaces also varies from region to region. Moreover, the surface quality after machining is an important factor because it imposes certain influences on the workpiece performance during application. Accordingly, the roughness of partition machined surfaces on the FGM specimen was measured and analyzed.

In this study, center line average height (R_a) was selected for evaluation. R_a is the arithmetic average of the absolute values of the profile height deviations from the mean line, recorded within the evaluation length. In particular, the surface roughness R_a in each gradient section was measured by a portable roughness tester (RUGOSURF 20, TESA TECHNOLOGY). Before the measurement, a calibration

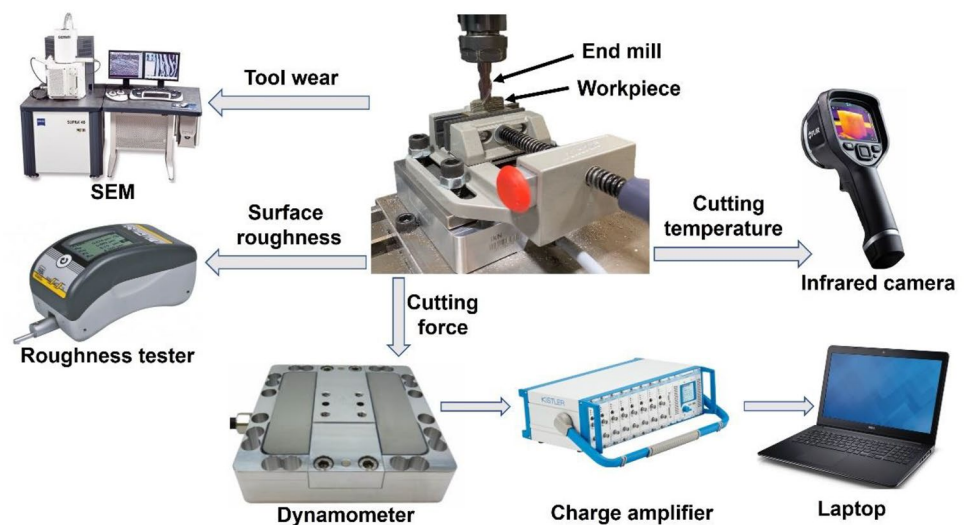
block was used to calibrate the tester so that more accurate test results could be collected. In each material composition region, R_a measurements were repeated ten times and all the results were recorded and used to construct boxplots (Fig. 3).

2.2.3 Cutting temperature measurement

During the metal cutting process, the source of cutting heat is machine energy transferred to heat through plastic deformation of the metal within the shear zone ahead of the cutting edge, as well as friction between the cutting tool face and the chip, and friction between the workpiece and the cutting tool [16]. The significant influences of milling temperature on machining performance make it an important factor for machining. Particularly, as the cutting temperature increases during milling, the tool strength tends to decrease, leading to faster tool wear or even failure. In addition, the high cutting temperature is also a reason for the severe workpiece material adhesion on the cutting tool faces. Moreover, tool wear due to too high cutting temperature brings about work hardening, as well as damage to and residual stress within the finished surfaces of workpiece, consistent with findings in previous studies where machined surface integrity and the machining precision were all directly affected by the cutting temperature [17].

During cutting, an infrared camera (FLIR E5-XT, Teledyne Technologies) was utilized to capture and record the temperature changes using a simple and visual non-contact method. Such infrared thermometers have been employed in more studies than any other cutting temperature measurement method. The main advantages of infrared sensors are their non-contact, swift responses to temperature changes, which enable readily accessible measurement of high temperatures without disturbing the heat distribution or being affected by cutting process [18]. Before the measurement,

Fig. 3 Setup for milling and the tests regarding machinability, depicting instruments for roughness, cutting temperature, cutting forces, and tool wear measurement



the instrument was placed in front of CNC machine and the detector of the infrared camera was focused on the machined regions. Figure 4 shows objects within the milling setup displayed as different colors according to the different temperature zones. In the partition milling strategy, the five sections corresponding respectively to the different material composition underwent successive milling, during which time temperature measurements were simultaneously recorded.

2.2.4 Cutting force investigation

For the force measurements, a 3-axis force dynamometer (ME-Meßsysteme GmbH, K3D120) with a range of ± 1 kN was used. This force dynamometer is capable of measuring the component cutting forces in the X, Y, and Z directions during machining of FGMs. The charge amplifier which was attached to the cutting force dynamometer converted the high-impedance charge input into a usable output voltage so that the real time cutting forces could be collected and sent to the PC. During the machining, the cutting forces along the three coordinate directions were collected and recorded separately in order to make more targeted analysis of the machinability of FGMs. Since the SS316L/IN718 FGM covered five material sections, there were five corresponding milling trials in total. Also, five measurements were conducted throughout the machining process where the setup employed for milling and cutting forces measurement was configured as shown in the earlier Fig. 3.

As mentioned in the previous section, the FGM specimens machined in this work exhibited a smooth transition from SS316L to IN718. Such material composition change is manifested in the mechanical properties as well. The key factors which apparently influence the cutting forces undoubtedly include the material hardness, cutting parameters, and even friction coefficient. As acknowledged, the cutting force

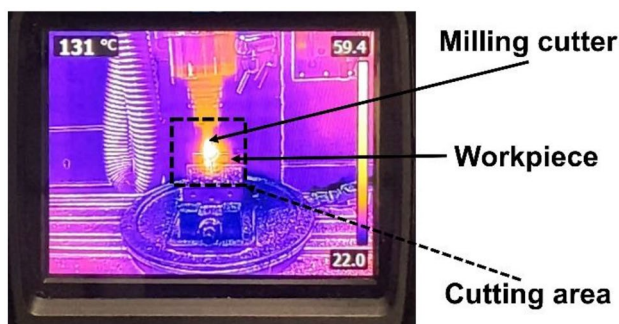


Fig. 4 Graphic user interface for infrared camera used to capture cutting temperature. The various colors represent corresponding temperature values. The cutting area is indicated by the black box wherein a bright spot shows the extremely high cutting temperature, while the regions with lower temperature such as the environment are shown by blue and purple colors

can pose a major concern to in milling operations with high surface quality requirements [19]. The fluctuation of cutting forces may impose adverse effects on surface quality and also the service life of the cutting tool [20]. To systematically investigate the machinability of FGMs, the cutting force is therefore a significant parameter that requires analysis.

2.2.5 Tool wear identification

For better study the machinability of FGMs, tool wear is of huge significance to be observed and analyzed. Since the FGMs showing gradually changed material properties are novel materials which were printed with two types of metal powder, the optimized machining scheme is still to be determined. The hardness of IN718 is higher than SS316L, while SS316L shows more plasticity than IN718 during machining processes. So, the machining performance of the material sections in FGMs might be different as well. In this situation, the tool wear mechanism which affects machining quality and even the tool life should be explored.

To identify the tool wear, each material section was conducted a milling operation with a new end mill and the same milling parameters. After milling operations, these end mills were observed under the SEM (DM07 Zeiss Supra 40 Scanning Electron Microscope) to identify the tool wear.

3 Results and discussion

3.1 Material composition gradients

After performing EDS tests on the specimen at the selected points, 10 EDS report maps were obtained. The EDS result of test point no. 1, located in the 100% SS316L section, is shown in Fig. 5a. The three primary elements with corresponding peaks (Fe, Ni, and Cr) are indicated. As shown in Fig. 5b, the weight ratios of the three elements were collected and are plotted at each test location. The Fe weight ratio gradually decreased as build height increased, while the weight ratio of Ni increased. Such a gradual variation of the elements is consistent with the gradient distribution expected.

However, according to the EDS results in Fig. 5b, the weight ratio of Ni in the 100% SS316L reached 18.15%, which is much higher than the normal value of 10 to 14%, as indicated in Table 1. Likewise, in the 100% IN718 section, the weight ratio of Fe also exceeded the balance amount in the alloy powder. The reason for such an unexpected feature of material distribution is caused by Marangoni convection that occurred during the DED process (Fig. 5c). When a specific layer of metal powder was melted by the laser, several previously deposited layers below the current layer also

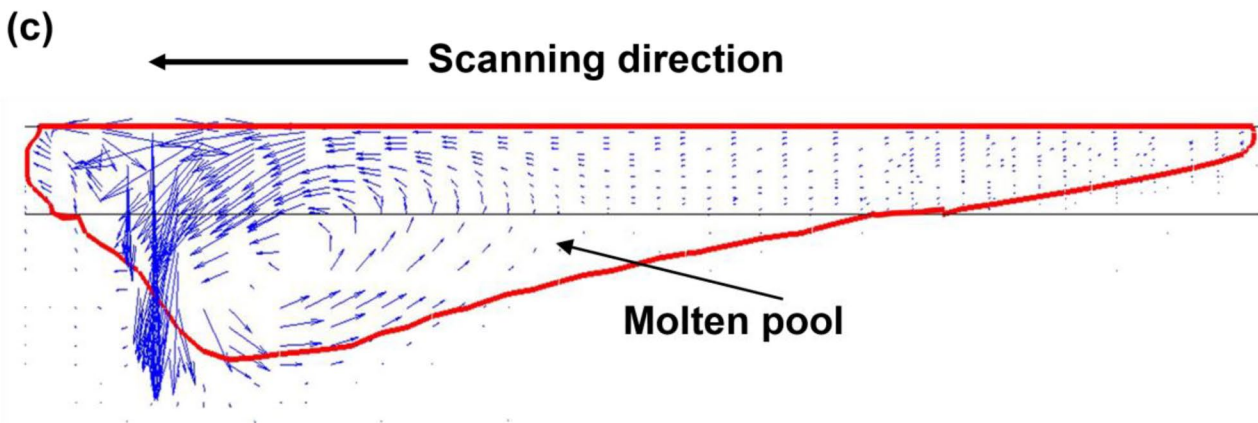
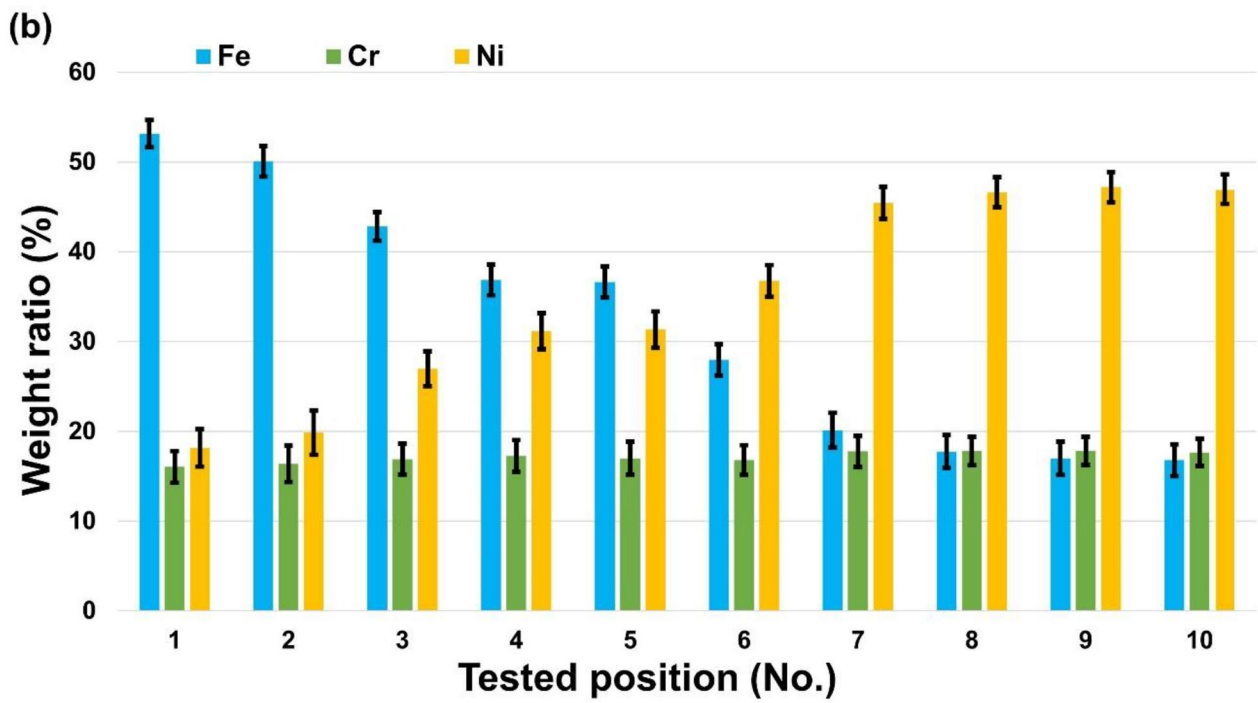
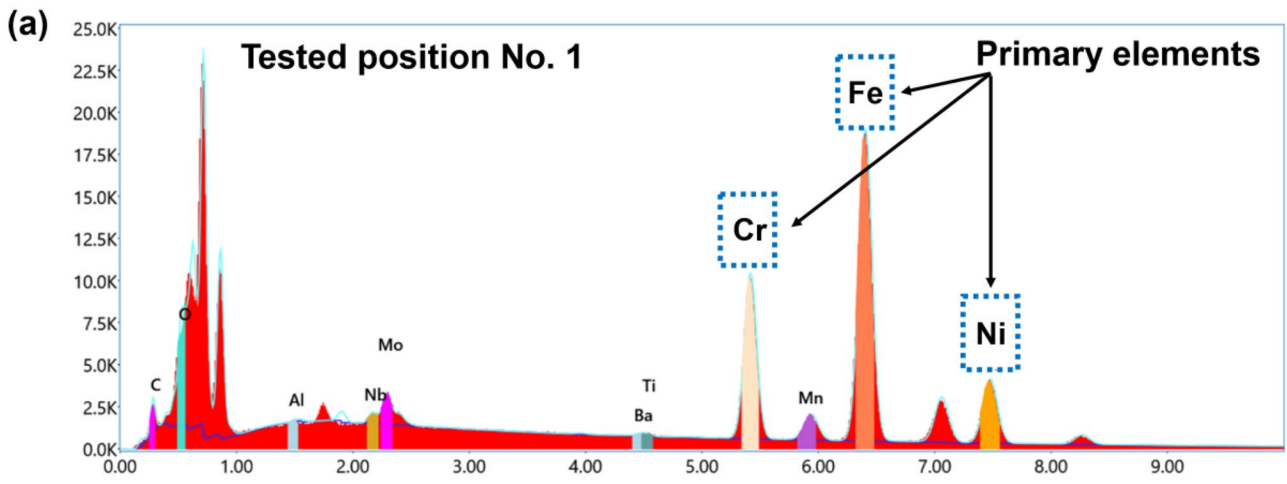


Fig. 5 **a** The EDS report map of test point no. 1, located in the 100% SS316L region (shown for illustrative purposes), in which the peaks of Fe, Ni, and Cr primary elements are labeled. **b** Weight ratios of the three primary elements at each test point location in the FGM build height, from which the increase in Ni and decrease in Fe are clearly demonstrated. **c** Model of Marangoni convection occurring in the molten pool with the inner fluid flow movement depicted [22]

experienced remelting wherein the Marangoni force lifted the material lying beneath while also transferring material in the upper layers to the lower layers. In particular, when Marangoni convection occurred in the boundary between 100% SS316L and 75% SS316L/25% IN718 sections, the fluid flow in the molten pool carried IN718 from the upper section where the weight ratio of Ni was 50 to 55% downward to the 100% SS316L section, which resulted in an increase of Ni in the 100% SS316L section. Similarly, some amount of SS316L was also inevitably transferred to the 100% IN718 region via fluid flow in the molten pool under the influence of Marangoni convection [21].

3.2 Surface roughness analysis

As shown in Fig. 6, the average roughness, R_a , increases from the 100% IN718 region to the 100% SS316L region as the content of SS316L rose. Such variation in R_a for the material gradient can be explained by the mechanism in which R_a decreases as a result of material hardness increase. It is acknowledged that the friction at the tool-specimen interface is influenced by the hardness of materials in that higher hardness tends to mitigate workpiece plasticity and the extent of lateral plastic flow. When the plastic deformation is reduced, the materials become easier to cut and correspondingly lead to smoother surfaces after milling [23, 24]. Among the five gradient regions, the 100% IN718 section had the highest hardness, commensurate with the lowest

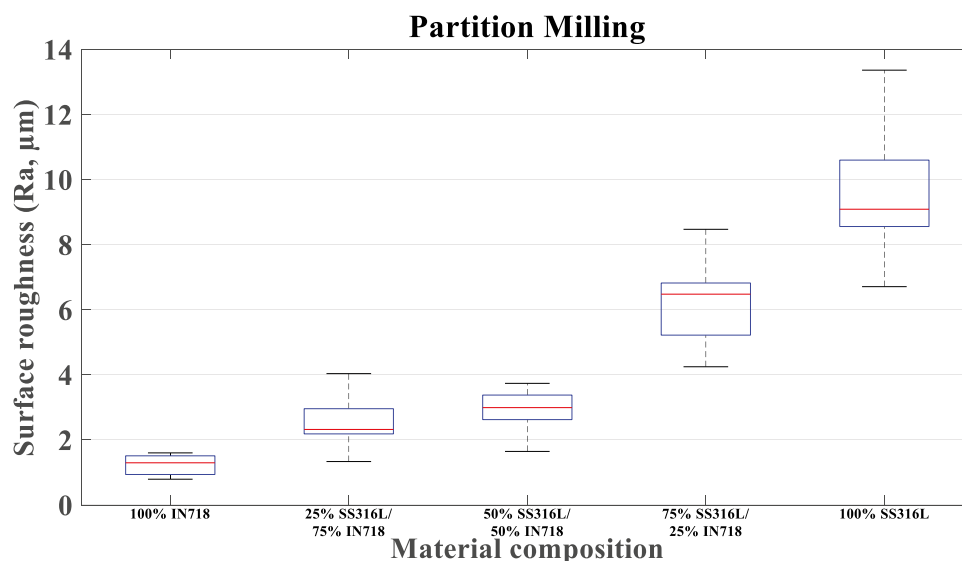
R_a value, while the 100% SS316L exhibited the highest R_a due to this region having the lowest hardness. For the other three sections between the top Section 100% IN718 and the 100% SS316L in the bottom, the surface roughness gradually increased as the content of SS316L increased, which was also induced by the increased plastic deformation.

3.3 Cutting temperature analysis

Through the infrared camera, the cutting temperature changes throughout the machining processes were easily observed and recorded. The images of the maximum cutting temperature of each gradient in FGMs were posted (Fig. 7–e). Besides, the cutting temperature of each material composition section were extracted and plotted by MATLAB as shown in Fig. 7f. Then, the maximum cutting temperature (T_m) that each section reached during partition milling was also shown in Fig. 7g. It can be seen that the temperature of each material section increased rapidly from room temperature as the workpiece was machined (Fig. 7f). Then, a cutting temperature reached an equilibrium stage. Each cutting round which started from tool-workpiece contact lasted about 78 s. Thus, there existed a specimen temperature dropping at the seventieth second as the cutting tool was separated from the workpiece.

Although the milling temperature variation tendencies of the five sections on FGM specimen were quite similar, some difference of cutting temperature of the five material sections can still be found, because the cutting temperature of different materials responds to machining processes differently. For example, the maximum cutting temperature captured in every milling trial of FGM specimen tended to increase as the content of IN718 in FGMs increase, as shown in Fig. 7g. Actually, T_m of each region should be different since the content ratio of the

Fig. 6 Boxplots of the surface roughness, R_a , for the different regions of the machined FGM workpiece with the partition milling strategy



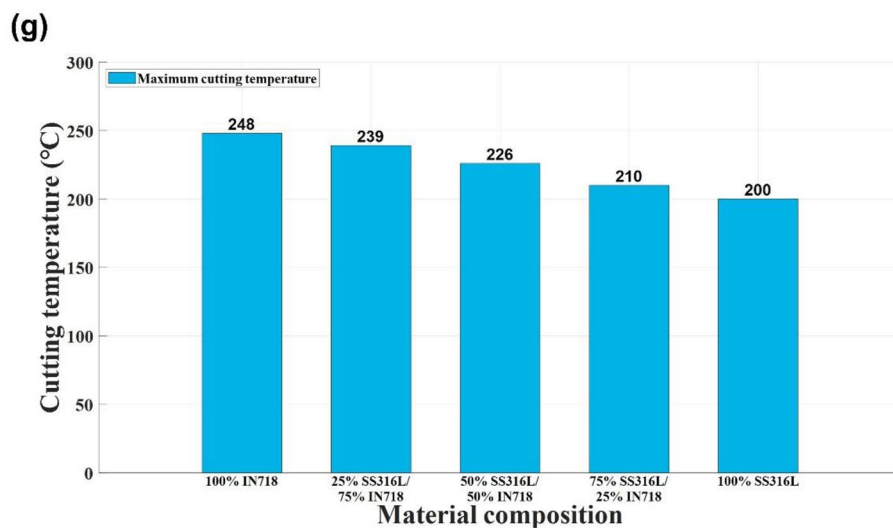
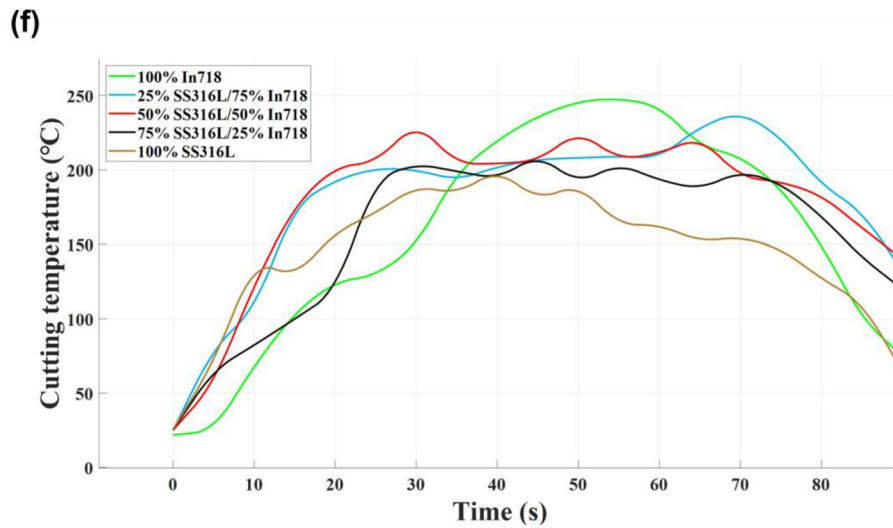
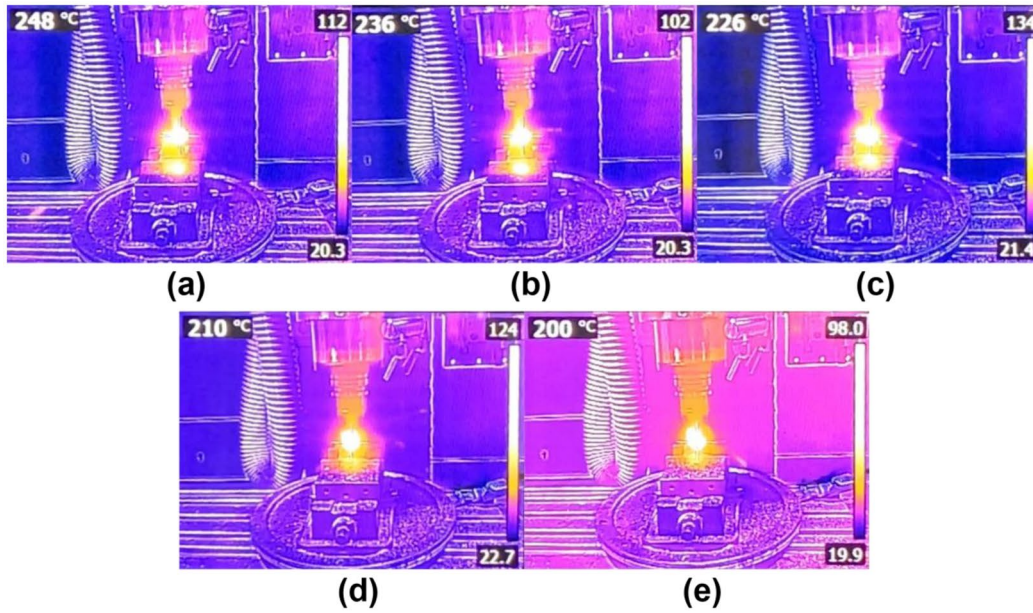


Fig. 7 a–e The infrared images that show the maximum cutting temperatures during the machining process of each material gradient from 100% IN718 on the top to the 100% SS316L at the bottom. **f** The temperature change of FGM specimen through the milling process. Five different colors were used to distinguish the five material sections containing different amount of IN718 and SS316L. **g** During milling the five SS316L and IN718 material regions with specific ratios, the maximum cutting temperatures that FGMs could reach were shown, in which the gradual reduction of maximum of cutting temperatures was easily observed

two materials, IN718 and SS316L, was designed to be distinguished a region from one another, which determined that the mechanical properties like hardness and strength were not the same values.

In Fig. 7g, it should be noted that the cutting tool and FGM specimen were exposed to a cutting temperature that was recorded as high as 248 °C, when milling operation was performed on the first material section containing 100% IN718. As the content of SS316L was increased to 25%, T_m of this region reached 239 °C which was lower than T_m of the 100% IN718 material section. Likewise, when the percentage of content of IN718 was reduced to 50% and 25% respectively, the maximum cutting temperature of the two machined regions were decreased to 226 °C and 210 °C. When the 100% SS 316L region was machined, T_m just reached 200 °C which was the lowest T_m in all the machined five regions. Thus, the maximum cutting temperature of each region exhibited a tendency to decrease with the proportion of SS316L growing.

Such a change of T_m can be explained by the different mechanical properties of IN718 and SS316L. Compared to SS316L, Inconel 718 alloy has lower machinability making machining of IN718 more challenging. This thermal resistant alloy combines high strength with strain hardening tendency, which induces high cutting forces and extreme cutting temperatures during the machining [25]. Additionally, IN718 alloy does not perform better than SS316L in the aspect of cutting heat dissipation due to the relatively lower heat conductivity of IN718. Therefore, T_m of a section was prone to be higher as the proportion of IN718 increases along the build-up orientation of the FGMs.

3.4 Cutting force analysis

The cutting distance of each material gradient was the same as the length of the FGM specimen, indicating that the milling transitioned from one end to the other. All force curves in the plots of Fig. 8 reveal a common trend in that the cutting force in x and y direction (F_x and F_y) rose initially then reached a full tool-workpiece contact cutting stage. Finally, the cutting forces rapidly reduced to zero at the end of each milling trial. Such a trend is quite similar to that of cutting temperature variation discussed above. This similarity in

trend for the cutting forces and cutting temperatures can be explained by the correlation between the two factors. When the end mill first contacted the workpiece, the cutting forces were the lowest as the cutting depth was equal to zero. However, when the cutting depth increased to a maximum, the forces reached their highest values and, correspondingly the friction (which was the main source of cutting heat) also reached its peak. As each milling trial approached its completion, the cutting force decreased and the friction between the end mill and FGMs dropped also, consistent with the decrease of cutting temperature toward the end of milling.

In addition, the fluctuations of forces in the milling passes were induced by the significant anisotropy in the irregular geometries, which is not uncommon in all 3D printed components [26, 27]. Thus, factors such as microhardness and cutting depth, which impact cutting performance, vary from point to point even in the same material gradient, and cause certain disturbances in the milling forces. Another aspect about cutting forces to be discussed is that the F_x tended to be generally higher than F_y in every cutting trial. The difference between F_x and F_y is because the feeding direction was selected as X -axis. So, the cutting tool necessarily overcame most resistance along X -axis while removing workpiece material, which made the cutting forces in the X -direction greater than in the Y -direction. Similarly, since little material was cut along Z -direction, the force component F_z , with subtle fluctuations, was justifiably the lowest among the three component forces.

Since the hardness of IN718 is much higher than that of SS316L, the hardness values along build-up direction gradually increased as the weight fraction of IN718 grew [28]. In other words, it was relatively easier for the end mill to cut materials composed of proportionally more SS316L. Consequently, it was indeed expected that the pure IN718 region in FGMs should present the highest forces as it has significantly higher strength and hardness than any other section [29, 30]. As Fig. 8f indeed shows, the maximum F_x and F_y of each material gradient increased along the build-up direction in which the weight fraction of IN718 was proportionally greater.

3.5 Tool wear mechanism

Tool wear occurs because tools and workpiece are contacting with sever friction, rubbing and huge stresses during machining. Also because of the high cutting temperature that the tools are subjected to, tool wear occurs gradually and leads to tool failure finally.

In this project, tool wear mechanism can be summarized through the results shown in the SEM images (Fig. 9). These tool wear images were captured with a 16 magnitude in the SEM. From the images on the right column in Fig. 9, it can be seen that the dominate tool wear mechanism was

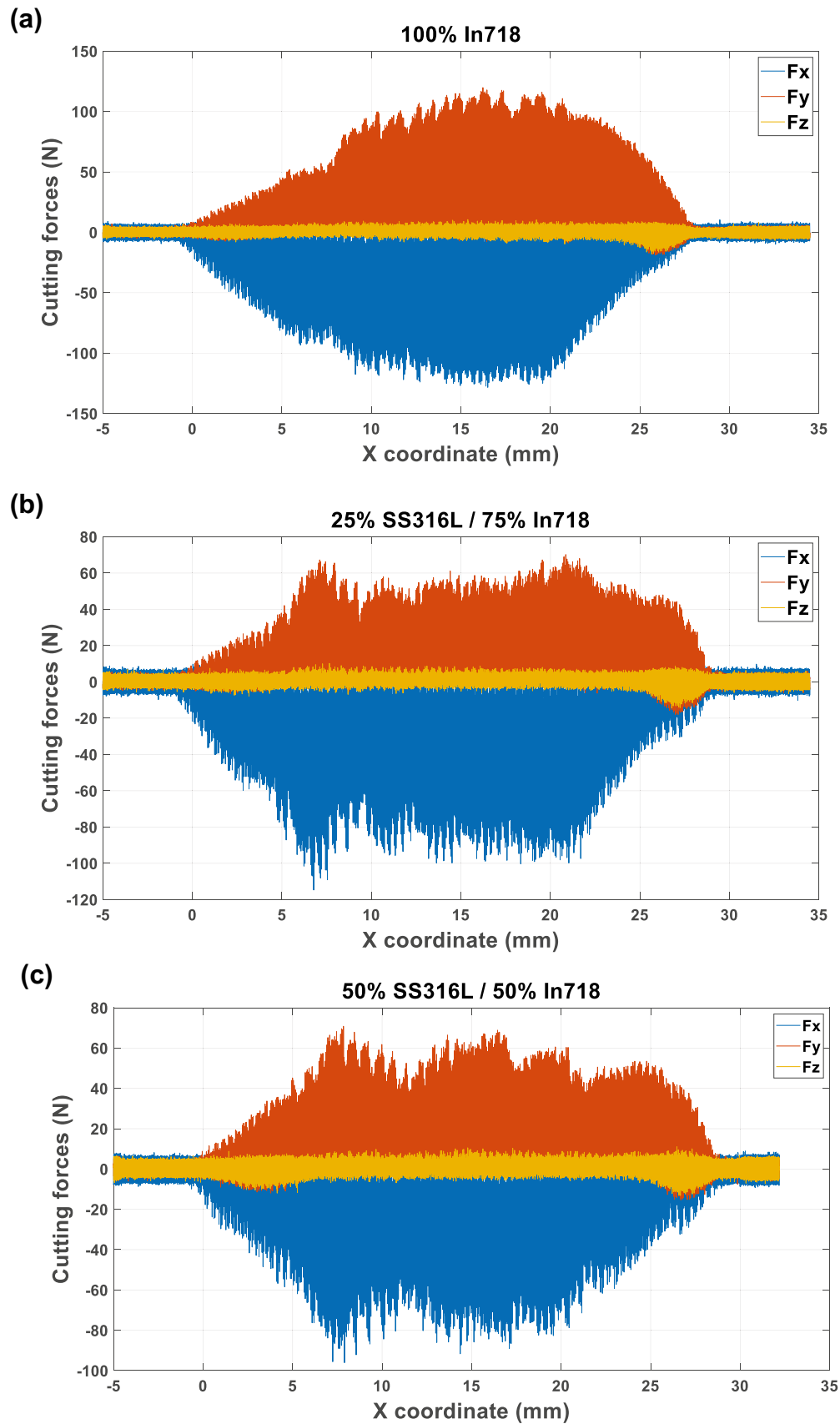


Fig. 8 a–e Cutting force results for all five material composition sections. f Maximum of cutting forces F_x and F_y in each of the corresponding five milling passes

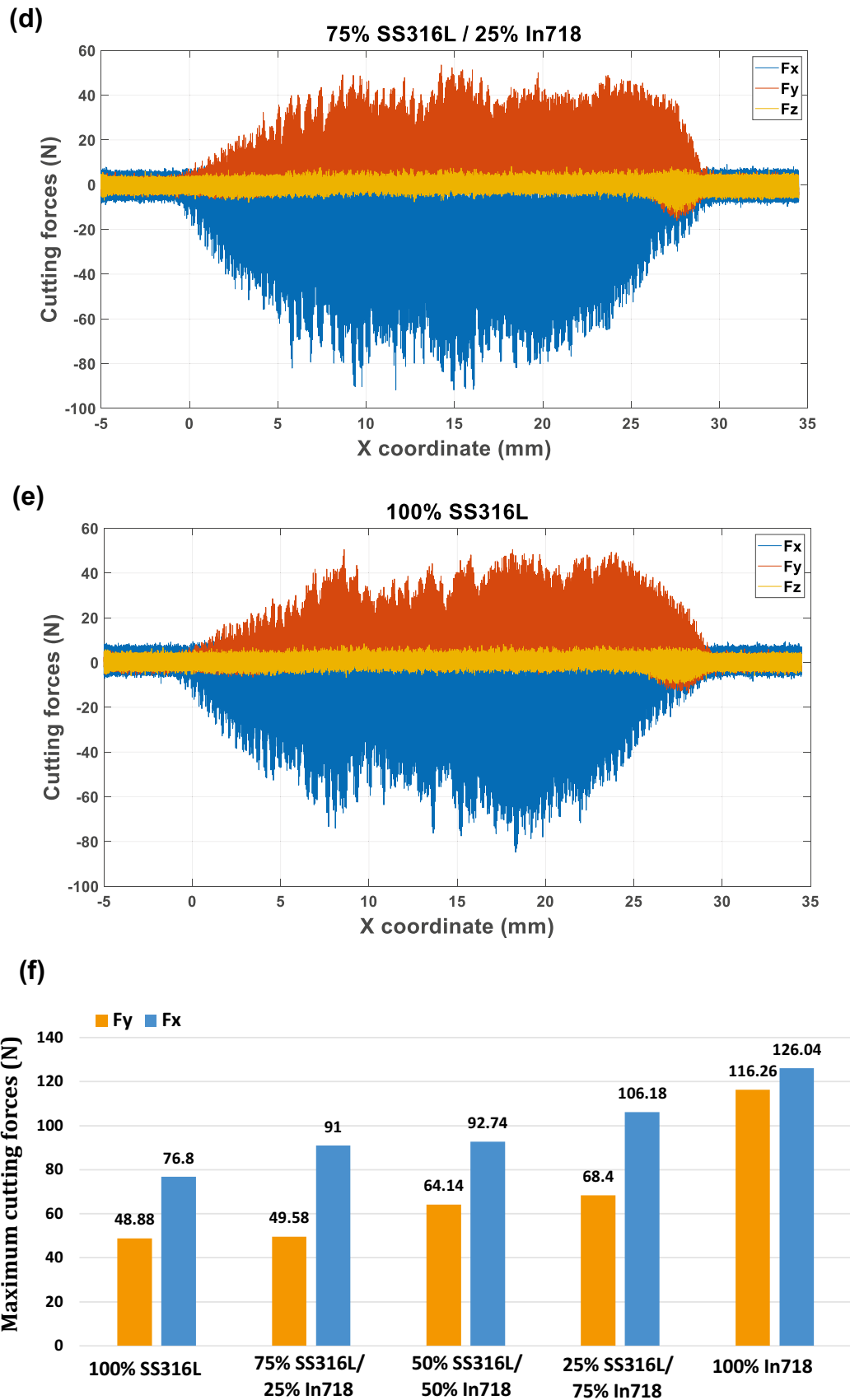
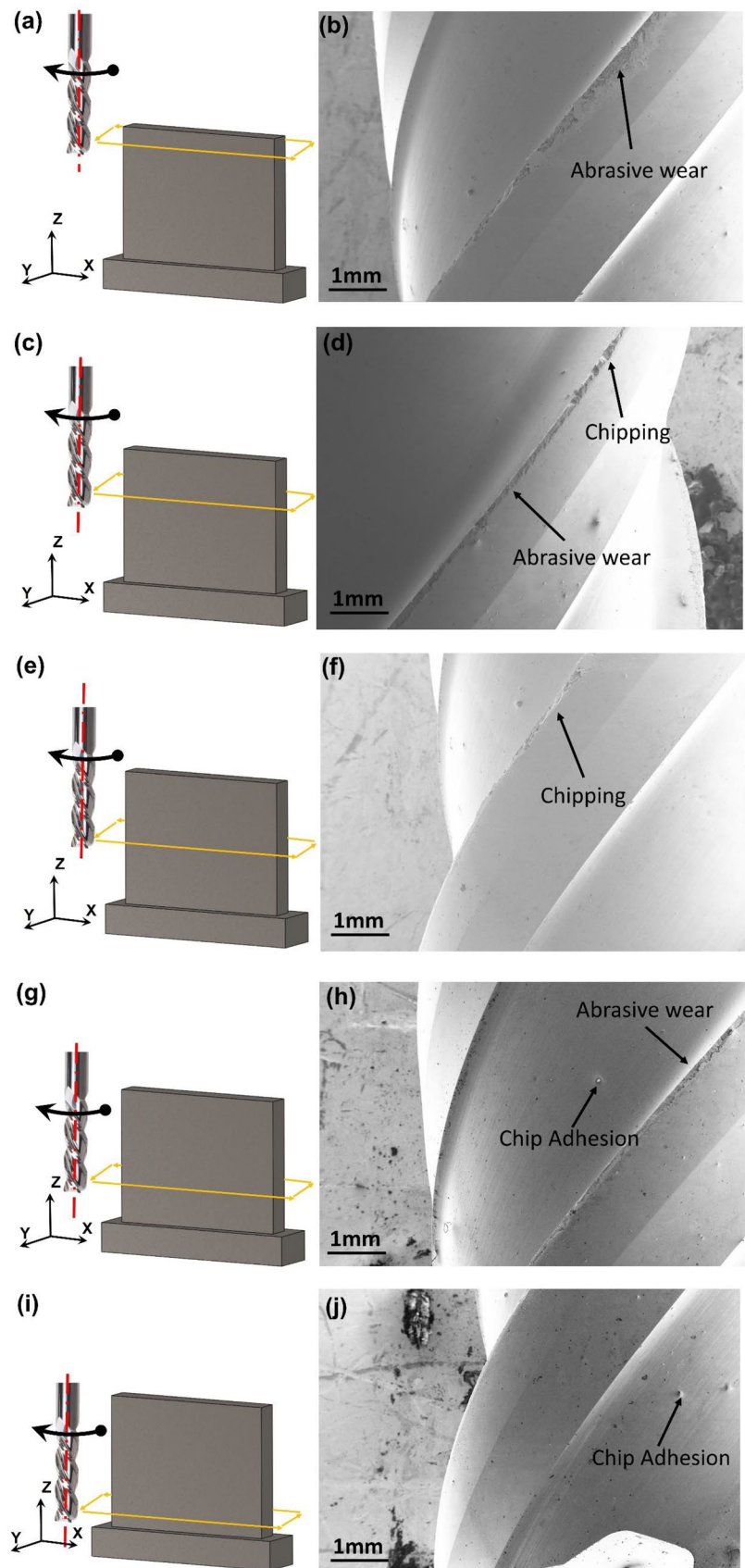


Fig. 8 (continued)

Fig. 9 **a, b** Milling 100% IN718 region and the tool wear. **c, d** Milling 25%SS316L + 75%IN718 region and the tool wear. **e, f** Milling 50%SS316L + 50%IN718 region and the tool wear. **g, h** Milling 75%SS316L + 25%IN718 region and the tool wear. **i, j** Milling 100%SS316L region and the tool wear



abrasive wear, while the diagrams on the left column show the machined material sections. Chip adhesion and even chipping were also found under the SEM. The abrasive wear was not observed in the region in the 100% SS316L region in which the hardness was lower than the regions containing IN718. Thus, in the regions which were printed with more IN718, the hardness increased and tool wear became more severe. Besides, the higher cutting forces and cutting temperature in the sections containing more IN718 also exacerbated the abrasive wear.

However, no significant difference of the wear degree of the five tools could be identified since the cutting distance in this project was not long enough to make the tool wear significantly severe. And such degree of tool wear on each end mill was not huge enough to negatively influence the surface roughness.

4 Conclusion

In this study, SS316L/IN718 FGM were fabricated by the DED technique, and the machinability of this innovative material type was investigated by performing milling type post-machining. Through consideration of material properties distributed in a gradient fashion and conducting a series of experimental tests consisting of EDS, machining temperatures, cutting forces and roughness of the machined surfaces and tool wear mechanism, the machinability of FGMs was concluded.

The EDS results confirmed that the overall material gradient was successfully formed since the main chemical elements comprising the two-component alloy regions revealed a gradient distribution along build direction. In the subsequent machinability tests, the surface roughness, machining temperatures, and cutting forces also presented gradual variations throughout the volume of FGM, which aligns with the mechanical properties transition. In particular, the sections containing comparatively more IN718 and less SS316L exhibited higher hardness and strength, which led them to present higher cutting forces and generate more cutting heat. Although higher contents of IN718 made end mills get wore easier due to higher hardness, cutting forces and cutting temperatures than 100% SS316L section, tool wear mechanism and size did not exhibit significant difference because of the short cutting distance. Furthermore, the lower plasticity was also a favorable factor that reduced plastic deformation during milling, helping to improve surface quality.

These new results can contribute to furthering the research and broadening the applications of FGMs.

Acknowledgements Li acknowledges the support of STARS funding from Texas.

Data availability Since the data is part of an ongoing study, it cannot be shared to reproduce the results.

Code availability Not applicable.

Declarations

Ethics approval Not applicable.

Consent to participate Not applicable.

Consent to publication Authors have agreed and provided consent for the published version of the manuscript.

Conflict of interest The authors declare no competing interests.

References

- Kar J, Roy SK, Roy GG (2016) Effect of beam oscillation on electron beam welding of copper with AISI-304 stainless steel. *J Mater Process Technol* 233:174–185. <https://doi.org/10.1016/j.jmatprotec.2016.03.001>
- Ghanavati R, Naffakh-Moosavy H, Moradi M (2021) Additive manufacturing of thin-walled SS316L-IN718 functionally graded materials by direct laser metal deposition. *J Market Res* 15:2673–2685. <https://doi.org/10.1016/j.jmrt.2021.09.061>
- Ghanavati R, Naffakh-Moosavy H (2021) Additive manufacturing of functionally graded metallic materials: A review of experimental and numerical studies. *J Market Res* 13:1628–1664. <https://doi.org/10.1016/j.jmrt.2021.05.022>
- Ahn D-G (2021) Directed Energy Deposition (DED) Process: state of the art. *Int J of Precis Eng Manuf-Green Tech* 8:703–742. <https://doi.org/10.1007/s40684-020-00302-7>
- Li P, Gong Y, Xu Y et al (2019) Inconel-steel functionally bimetal materials by hybrid directed energy deposition and thermal milling: microstructure and mechanical properties. *Arch Civil Mech Eng* 19:820–831. <https://doi.org/10.1016/j.acme.2019.03.002>
- Kim SH, Lee H, Yeon SM et al (2021) Selective compositional range exclusion via directed energy deposition to produce a defect-free Inconel 718/SS 316L functionally graded material. *Addit Manuf* 47:102288. <https://doi.org/10.1016/j.addma.2021.102288>
- Banait SM, Paul CP, Jinoop AN et al (2020) Experimental investigation on laser directed energy deposition of functionally graded layers of Ni-Cr-B-Si and SS316L. *Opt Laser Technol* 121:105787. <https://doi.org/10.1016/j.optlastec.2019.105787>
- Khaliq W, Zhang C, Jamil M, Khan AM (2020) Tool wear, surface quality, and residual stresses analysis of micro-machined additive manufactured Ti-6Al-4V under dry and MQL conditions. *Tribol Int* 151:106408. <https://doi.org/10.1016/j.triboint.2020.106408>
- Woo W-S, Kim E-J, Jeong H-I, Lee C-M (2020) Laser-assisted machining of Ti-6Al-4V fabricated by DED additive manufacturing. *Int J of Precis Eng Manuf-Green Tech* 7:559–572. <https://doi.org/10.1007/s40684-020-00221-7>
- Zhang H, Dang J, Ming W et al (2020) Cutting responses of additive manufactured Ti6Al4V with solid ceramic tool under dry

- high-speed milling processes. *Ceram Int* 46:14536–14547. <https://doi.org/10.1016/j.ceramint.2020.02.253>
11. Lizzul L, Sorgato M, Bertolini R et al (2020) Influence of additive manufacturing-induced anisotropy on tool wear in end milling of Ti6Al4V. *Tribol Int* 146:106200. <https://doi.org/10.1016/j.triboint.2020.106200>
 12. Ming W, Chen J, An Q, Chen M (2019) Dynamic mechanical properties and machinability characteristics of selective laser melted and forged Ti6Al4V. *J Mater Process Technol* 271:284–292. <https://doi.org/10.1016/j.jmatprotec.2019.04.015>
 13. Yong CK, Gibbons GJ, Wong CC, West G (2020) A critical review of the material characteristics of additive manufactured IN718 for high-temperature application. *Metals* 10:1576. <https://doi.org/10.3390/met10121576>
 14. Lorenz KA, Jones JB, Wimpenny DI, Jackson MR (2015) A review of hybrid manufacturing. 13
 15. Sinha MK, Madarkar R, Ghosh S, Rao PV (2017) Application of eco-friendly nanofluids during grinding of Inconel 718 through small quantity lubrication. *J Clean Prod* 141:1359–1375. <https://doi.org/10.1016/j.jclepro.2016.09.212>
 16. Sun Y, Sun J, Li J, Xiong Q (2014) An experimental investigation of the influence of cutting parameters on cutting temperature in milling Ti6Al4V by applying semi-artificial thermocouple. *Int J Adv Manuf Technol* 70:765–773. <https://doi.org/10.1007/s00170-013-5294-1>
 17. Longbottom JM, Lanham JD (2005) Cutting temperature measurement while machining – a review. *Aircr Eng Aerosp Technol* 77:122–130. <https://doi.org/10.1108/00022660510585956>
 18. Suhail AH et al (2010) Optimization of cutting parameters based on surface roughness and assistance of workpiece surface temperature in turning process. *Am J Eng Appl Sci* 3:102–108. <https://doi.org/10.3844/ajeassp.2010.102.108>
 19. Qiao G, Zhang B, Bai Q et al (2022) Machinability of TiC-reinforced titanium matrix composites fabricated by additive manufacturing. *J Manuf Process* 76:412–418. <https://doi.org/10.1016/j.jmapro.2022.02.033>
 20. Suresh Kumar Reddy N, Venkateswara Rao P (2006) Experimental investigation to study the effect of solid lubricants on cutting forces and surface quality in end milling. *Int J Mach Tools Manuf* 46:189–198. <https://doi.org/10.1016/j.ijmachtools.2005.04.008>
 21. Li W, Karnati S, Kriewall C et al (2017) Fabrication and characterization of a functionally graded material from Ti-6Al-4V to SS316 by laser metal deposition. *Addit Manuf* 14:95–104. <https://doi.org/10.1016/j.addma.2016.12.006>
 22. Le T-N, Lo Y-L (2019) Effects of sulfur concentration and Marangoni convection on melt-pool formation in transition mode of selective laser melting process. *Mater Des* 179:107866. <https://doi.org/10.1016/j.matdes.2019.107866>
 23. Al-Rubaie KS, Melotti S, Rabelo A et al (2020) Machinability of SLM-produced Ti6Al4V titanium alloy parts. *J Manuf Process* 57:768–786. <https://doi.org/10.1016/j.jmapro.2020.07.035>
 24. Yassin A, Ueda T, Furumoto T et al (2009) Experimental investigation on cutting mechanism of laser sintered material using small ball end mill. *J Mater Process Technol* 209:5680–5689. <https://doi.org/10.1016/j.jmatprotec.2009.05.029>
 25. Pereira O, Celaya A, Urbikain G et al (2020) CO2 cryogenic milling of Inconel 718: cutting forces and tool wear. *J Market Res* 9:8459–8468. <https://doi.org/10.1016/j.jmrt.2020.05.118>
 26. Oyelola O, Jackson-Crisp A, Crawforth P et al (2020) Machining of directed energy deposited Ti6Al4V using adaptive control. *J Manuf Process* 54:240–250. <https://doi.org/10.1016/j.jmapro.2020.03.004>
 27. Cus F, Zuperl U, Kiker E, Milfelner M (2006) Adaptive controller design for feedrate maximization of machining process. *J Achievements Mater Manuf Eng* 17:4
 28. Zhang R, Nagaraja KM, Bian N et al (2022) Experimental studies on fabricating functionally gradient material of stainless steel 316L-Inconel 718 through hybrid manufacturing: directed energy deposition and machining. *Int J Adv Manuf Technol*. <https://doi.org/10.1007/s00170-022-09304-y>
 29. de Oliveira CF, Araujo AC, Jardini Munhoz AL, Kapoor SG (2020) The influence of additive manufacturing on the micro-milling machinability of Ti6Al4V: A comparison of SLM and commercial workpieces. *J Manuf Process* 60:299–307. <https://doi.org/10.1016/j.jmapro.2020.10.006>
 30. Polishetty A, Shunmugavel M, Goldberg M et al (2017) Cutting force and surface finish analysis of machining additive manufactured titanium alloy Ti-6Al-4V. *Procedia Manuf* 7:284–289. <https://doi.org/10.1016/j.promfg.2016.12.071>

Publisher's Note Springer Nature remains neutral with regard to jurisdictional claims in published maps and institutional affiliations.

Springer Nature or its licensor holds exclusive rights to this article under a publishing agreement with the author(s) or other rightsholder(s); author self-archiving of the accepted manuscript version of this article is solely governed by the terms of such publishing agreement and applicable law.